Supplementary Information for "Physics-Based Thermal Reduced-Order Models for Battery Pack Health Monitoring: Application to NASA's X-57 Electric Aircraft"

Michael Khasin[1], Mohit R. Mehta[2], John W. Lawson[1]

[1]Intelligent Systems Division, NASA Ames Research Center, Moffett Field, CA 94035, USA
[2]KBR Inc., Intelligent Systems Division, NASA Ames Research Center, Moffett Field, CA 94035, USA

Contents

S1 Detailed Simulated Flight Profile (SFP) Mission Segments **1**

S2 Effective Thermal Properties and Timescale Analysis **2**
S2.1 Geometric and Material Properties . . . 2
S2.2 Volume Fraction Calculation . . . 2
S2.3 Effective Thermal Properties . . . 3
S2.4 External Heat Transfer Coefficient . . . 4
S2.5 Biot Number and Cooling Time . . . 4

S3 Adaptive Soft-Mode MBAM (AS-MBAM) **5**
S3.1 Information-Geometric Interpretation and Local Valley Picture . . . 5
S3.2 Geodesic MBAM and First-Order AS-MBAM . . . 6
S3.3 Bidirectional Candidate Generation and the Branching Tree . . . 6
S3.4 Application to the X-57 Six-Parameter Model . . . 7
S3.5 State and First-Order Sensitivity Equations, Relative Scaling, and the Discrete Metric 8

S4 Intermediate Per-Sensor ROMs for the X-57 Data **10**
S4.1 Resolution of the Structural Non-Identifiability . . . 10
S4.2 The $\tau_a \to 0$ Limit and the Six-Parameter ROM . . . 11

S1 Detailed Simulated Flight Profile (SFP) Mission Segments

The compact summary of the Simulated Flight Profile (SFP) given in the main text (Fig. 2 of the main paper; Section 2.2) is here expanded into the full mission-segment breakdown defined in Ref. [1]. The total mission requires a predicted 46.2 kW h of energy and involves a peak power draw of approximately 145 kW. The brick-level current trace shown in Fig. 2 of the main paper corresponds to the recorded laboratory evaluation window used for model fitting; the low-power taxi segments listed below lie outside that recorded window.

1. **Ground Operations (Taxi).** The mission begins with a 600 s taxi from the hangar, imposing a low-power draw of 2.15 W per cell. This is followed by a 120 s checklist period with zero power draw.

2. **Takeoff Sequence.** Preparations for takeoff involve a 30 s cruise runup, which places a high demand on the cells at 25.76 W each. After a 60 s hold period with zero power, the aircraft proceeds with a 100 s ground roll and initial climb, drawing the same high power of 25.76 W per cell.

3. **Climb and Cruise.** The climb to cruise altitude is the most sustained high-power phase, lasting 540 s at a constant 25.76 W per cell. Following this, the aircraft enters a 300 s cruise phase where the power demand reduces to 19.32 W per cell.

4. **Descent and Approach.** A 450 s descent follows, with a further reduction in power to 12.88 W per cell. The final approach is a 180 s period of zero power draw.

5. **Go-Around and Final Landing.** The profile includes a simulated go-around manoeuvre, representing a safety-critical scenario. This involves a 90 s climb at the high-power draw of 25.76 W per cell, followed by a 90 s approach pattern at the cruise power of 19.32 W per cell. The mission concludes with another 180 s final approach (zero power), a 60 s rollout at 3.22 W per cell, and a final 600 s taxi back to the hangar at 2.15 W per cell.

The evaluation dataset analyzed in this paper is one SFP discharge of a single X-57 pack performed in a laboratory test at room ambient temperature, with sensor data sampled at 0.5 Hz. All 128 parallel-connected cell groups ("bricks") of that pack contribute to the per-brick analysis presented in the main text. Following Section 2.1 of the main paper, "pack" denotes the 2560-cell, 20P128S assembly of 128 series-connected bricks, which Ref. [1] calls a "single battery"; the aircraft battery system comprises two such packs in parallel. This single-profile dataset supports pack-wide fit evaluation. Repeated-profile studies will address cross-mission transfer and prognostic validation.

S2 Effective Thermal Properties and Timescale Analysis

This section provides the detailed derivation that supports the brief thermal-analysis summary given in Section 3 of the main paper. The analysis establishes the effective thermal properties of the sub-module's composite material and uses them to estimate the relevant timescales, justifying both the 2D treatment and the quasi-adiabatic approximation.

S2.1 Geometric and Material Properties

The sub-module is modeled as a composite of 18650 Li-ion cells embedded within an aluminum (6061 alloy) matrix. The base dimensions and standard material properties used in this analysis, derived from established engineering sources, are listed in Table S1.

S2.2 Volume Fraction Calculation

The volume fractions of the battery cells and the aluminum matrix are determined from the sub-module's geometry, estimated from the CAD images in Ref. [1].

1. **Sub-module footprint.** The CAD images show a 16×10 array of cells (Table 1 of the main paper). Using the cell diameter ($D = 18$ mm) as a scale, the inter-cell distance (aluminum

Table S1: Assumed physical and thermal properties of sub-module components. Values for 18650 cells represent typical bulk properties reported in literature, while values for Aluminum 6061 are for a standard T6 temper.

Property	**Symbol**	**18650 Li-ion cell**	**Aluminum (6061-T6)**
Density	ρ	$2200\,\mathrm{kg\,m^{-3}}$	$2700\,\mathrm{kg\,m^{-3}}$
Specific heat	c_p	$1100\,\mathrm{J\,kg^{-1}\,K^{-1}}$	$900\,\mathrm{J\,kg^{-1}\,K^{-1}}$
Thermal conductivity	k	$5\,\mathrm{W\,m^{-1}\,K^{-1}}$	$170\,\mathrm{W\,m^{-1}\,K^{-1}}$
Cell diameter	D_{cell}	18 mm	–
Sub-module thickness	t	0.1 m	
Cell count	N_{cells}	160 (20P8S)	

web thickness) is estimated to be approximately 2 mm, giving an effective center-to-center cell pitch of 20 mm:

$$\text{Width} \approx 16 \text{ cells} \times 20\,\text{mm/cell} = 320\,\text{mm} = 0.32\,\text{m}$$
$$\text{Depth} \approx 10 \text{ cells} \times 20\,\text{mm/cell} = 200\,\text{mm} = 0.2\,\text{m}$$

2. **Total sub-module volume.**

$$V_{\mathrm{total}} = \text{Width} \times \text{Depth} \times t = 0.32\,\mathrm{m} \times 0.2\,\mathrm{m} \times 0.1\,\mathrm{m} = 0.0064\,\mathrm{m^3}.$$

The footprint area, $0.064\,\mathrm{m^2}$, is fixed by the cell count and pitch and does not depend on the array aspect ratio.

3. **Volume of a single cell inclusion** (cylindrical column through the thickness):

$$V_{1\mathrm{cell}} = \pi \left(\frac{D_{\mathrm{cell}}}{2}\right)^2 \cdot t = \pi \left(\frac{0.018\,\mathrm{m}}{2}\right)^2 \cdot 0.1\,\mathrm{m} \approx 2.5 \times 10^{-5}\,\mathrm{m^3}.$$

4. **Total cell and aluminum volumes.**

$$V_{\mathrm{cells}} = N_{\mathrm{cells}} V_{1\mathrm{cell}} = 160 \cdot 2.5 \times 10^{-5}\,\mathrm{m^3} \approx 4.1 \times 10^{-3}\,\mathrm{m^3},$$

$$V_{\mathrm{Al}} = V_{\mathrm{total}} - V_{\mathrm{cells}} \approx 2.3 \times 10^{-3}\,\mathrm{m^3}.$$

5. **Volume fractions.**

$$\phi_{\mathrm{cells}} \approx 0.64\ (64\%), \qquad \phi_{\mathrm{Al}} \approx 0.36\ (36\%).$$

S2.3 Effective Thermal Properties

Effective density. The volume-weighted average gives

$$\rho_{\mathrm{eff}} = \phi_{\mathrm{Al}}\rho_{\mathrm{Al}} + \phi_{\mathrm{cells}}\rho_{\mathrm{cell}} = (0.36)(2700) + (0.64)(2200) \approx 2400\,\mathrm{kg\,m^{-3}}.$$

Effective specific heat. The mass-weighted average gives, with mass fractions $w_{\mathrm{Al}} \approx 0.41$ and $w_{\mathrm{cells}} \approx 0.59$,

$$c_{p,\mathrm{eff}} = w_{\mathrm{Al}} c_{p,\mathrm{Al}} + w_{\mathrm{cells}} c_{p,\mathrm{cell}} = (0.41)(900) + (0.59)(1100) \approx 1.0 \times 10^3\,\mathrm{J\,kg^{-1}\,K^{-1}}.$$

Anisotropic thermal conductivity. For heat flow perpendicular to the plate (along the cell axes), the aluminum matrix and the cells act as parallel thermal resistors:

$$k_{\text{eff},\perp} = \phi_{\text{Al}} k_{\text{Al}} + \phi_{\text{cells}} k_{\text{cell}} = (0.36)(170) + (0.64)(5) \approx 64\,\text{W m}^{-1}\,\text{K}^{-1}.$$

For heat flow parallel to the plate, the lower-conductivity cell inclusions obstruct the heat path through the matrix. Because the aluminum honeycomb forms a continuous, highly conductive web that completely embeds the cells, the in-plane conductivity is estimated by the Hashin–Shtrikman upper bound [2] for a 2D composite, which applies when the higher-conductivity phase is continuous:

$$k_{eff,||} = k_{Al} \frac{k_{cell} + k_{Al} + \phi_{cells}(k_{cell} - k_{Al})}{k_{cell} + k_{Al} - \phi_{cells}(k_{cell} - k_{Al})} \approx 170 \cdot \frac{175 - 106}{175 + 106} \approx 42 W m^{-1} K^{-1}. \tag{S1}$$

S2.4 External Heat Transfer Coefficient

With a representative laboratory ambient of $T_{\text{cold}} = 20\,^{\circ}\text{C}$ and a maximal sub-module surface temperature of $T_{\text{hot}} \approx 50\,^{\circ}\text{C}$, the two dominant external mechanisms are estimated as follows.

Natural convection. For a sub-module simplified to a plate whose characteristic linear dimension is its longer side, $\sim 0.32\,\text{m}$, the Grashof number is $Gr \approx 1.5 \times 10^8$ and the Rayleigh number is $Ra = Gr\,Pr \approx 1 \times 10^8$, below the laminar–turbulent transition at $Ra \approx 10^9$. The Churchill–Chu laminar correlation [3] gives $h_{\text{conv}} \approx 4.1$–$4.7\,\text{W m}^{-2}\,\text{K}^{-1}$ for characteristic lengths between the longer ($0.32\,\text{m}$) and shorter ($0.2\,\text{m}$) sides. We adopt the rounded-up value

$$h_{\text{conv}} \approx 5\,\text{W m}^{-2}\,\text{K}^{-1},$$

which overestimates the external heat loss and therefore provides a conservative basis for the quasi-adiabatic approximation below.

Linearized thermal radiation. With surface emissivity $\epsilon \approx 0.8$ (a reasonable value for an engineered surface), the linearized radiation coefficient is

$$h_{\text{rad}} = \epsilon\sigma\,(T_{\text{hot}}^2 + T_{\text{cold}}^2)(T_{\text{hot}} + T_{\text{cold}}) \approx 5\,\text{W m}^{-2}\,\text{K}^{-1}.$$

Radiation is therefore as significant as natural convection. The total external heat-transfer coefficient is

$$h_{\text{total}} = h_{\text{conv}} + h_{\text{rad}} \approx 10\,\text{W m}^{-2}\,\text{K}^{-1}.$$

These estimates apply to the laboratory evaluation environment. Flight-specific ambient temperature, airflow, and ventilation require re-evaluation of the corresponding effective heat-transfer coefficients.

S2.5 Biot Number and Cooling Time

Biot number across the thickness. To assess gradients across the sub-module thickness, the appropriate characteristic length is the thickness itself, $L_c = t = 0.1\,\text{m}$, and the appropriate conductivity is the perpendicular value $k_{\text{eff},\perp}$:

$$Bi = \frac{h_{\text{total}}\,L_c}{k_{\text{eff},\perp}} = \frac{(10\,\text{W m}^{-2}\,\text{K}^{-1})\,(0.1\,\text{m})}{64\,\text{W m}^{-1}\,\text{K}^{-1}} \approx 0.016 \;\ll\; 0.1. \tag{S2}$$

The small Biot number confirms that internal thermal resistance across the thickness is negligible compared to the external resistance to heat transfer, validating a 2D in-plane treatment of the sub-module.

External cooling time. By symmetry with the adjacent sub-module, cooling is assumed to occur from only one of the two large faces. The characteristic external cooling time is then

$$\tau_{\text{ext}} = \frac{\rho_{\text{eff}}\, c_{p,\text{eff}}\, L_c}{h_{\text{total}}} = \frac{(2400\,\text{kg m}^{-3})(1.0\times10^{3}\,\text{J kg}^{-1}\,\text{K}^{-1})(0.1\,\text{m})}{10\,\text{W m}^{-2}\,\text{K}^{-1}} \approx 2.4\times10^{4}\,\text{s} \approx 6.7\,\text{h}. \tag{S3}$$

Since the SFP discharge analyzed in the main text lasts only ~ 1 h, τ_{ext} is roughly seven times the mission duration. Together with the symmetry-induced adiabatic condition at the boundary with the adjacent sub-module, this justifies treating the sub-module as quasi-adiabatic for the purposes of single-mission thermal modeling.

This conclusion is robust to modest uncertainty in the external heat-transfer coefficient. If h_{total} varies by a factor of two, from 5 to 20 $\text{W m}^{-2}\,\text{K}^{-1}$, the Biot number spans approximately 0.008 to 0.031, remaining well below the usual lumped-thickness threshold $Bi \lesssim 0.1$. Over the same range, the external cooling time spans approximately 13.4 h to 3.4 h, still several times longer than the single-SFP evaluation window. Thus the 2D and quasi-adiabatic approximations are robust at the order-of-magnitude level for the laboratory test analyzed here. The conclusion is equally insensitive to the estimated composite properties. A $\pm20\%$ change in the cell volume fraction ϕ_{cells} gives $k_{\text{eff},\perp} \approx 43$–$86\,\text{W m}^{-1}\,\text{K}^{-1}$ and $Bi \approx 0.012$–0.023; Bi reaches 0.1 only for $k_{\text{eff},\perp} \approx 10\,\text{W m}^{-1}\,\text{K}^{-1}$, which would require an almost aluminum-free matrix. Over the same range the heat capacity per unit volume $\rho_{\text{eff}}c_{p,\text{eff}}$ changes by less than 1%, so τ_{ext} is unchanged. A $\pm20\%$ change in k_{cell} changes $k_{\text{eff},\perp}$ by about 1%.

These two results—$Bi \approx 0.016$ and $\tau_{\text{ext}} \approx 6.7$ h—are the basis of the brief summary statement made in the main text.

S3 Adaptive Soft-Mode MBAM (AS-MBAM)

This section gives the methodological detail that supports the concise candidate-discovery description in Section 5.3 of the main paper.

S3.1 Information-Geometric Interpretation and Local Valley Picture

For a normalized residual vector $r(q)$, the model maps the parameter coordinates q into residual space. The least-squares/Gauss–Newton sensitivity metric is

$$F_q(q) = J_q(q)^{\top} J_q(q), \qquad J_q = \frac{\partial r}{\partial q}. \tag{S4}$$

We use the conventional term Fisher Information Matrix (FIM) for F_q and use it as a local sensitivity metric. Its eigenvectors identify parameter combinations: a stiff direction produces a large first-order change in the normalized residuals, while a soft direction produces a small change.

For $C(q) = \frac{1}{2} r(q)^{\top} r(q)$, the Hessian—the matrix of second derivatives that describes the local curvature of the cost—is

$$H_C(q) \equiv \nabla_q^2 C(q) = J_q^{\top} J_q + \sum_a r_a(q)\, \nabla_q^2 r_a(q), \tag{S5}$$

where a indexes residual components. Near a good stationary fit, the residual-weighted second term is small, so $F_q = J_q^{\top} J_q$ is the Gauss–Newton approximation to the Hessian. AS-MBAM evaluates this first-order sensitivity metric. For a unit eigenvector v of $F_q(q_0)$ with eigenvalue λ,

$$C(q_0 + \delta v) - C(q_0) \simeq \frac{1}{2}\lambda\delta^2. \tag{S6}$$

The smallest-eigenvalue direction is therefore the locally least costly quadratic direction at the best fit. Away from the best fit, the same eigenvector minimizes the first-order residual change $\|J_q \delta v\|$ among unit directions in the selected coordinates.

Figure 5 of the main paper illustrates this local, two-dimensional picture; the full continuation is generated by re-evaluating the soft direction as the parameters evolve.

S3.2 Geodesic MBAM and First-Order AS-MBAM

Standard MBAM integrates a geodesic of the FIM-induced metric. Updating that path requires directional second-order output information, obtained through second-order sensitivity equations, automatic differentiation, or finite differences [4, 5].

AS-MBAM instead re-evaluates the smallest-eigenvalue direction of the first-order sensitivity metric along the continuation. The sensitivities used for fitting and identifiability analysis therefore also define the reduction path, reducing derivative-code, finite-difference, and verification requirements. Both MBAM and AS-MBAM can launch the search in the two orientations of a soft eigenvector [6]; their mathematical difference is the subsequent path update. Candidate endpoints are converted into analytical reduced models and assessed by independent refitting, prediction accuracy, and identifiability.

The relative-coordinate flow used in this work is

$$\frac{dq}{ds} = \frac{v_{\min}^{(q)}(q)}{\|v_{\min}^{(q)}(q)\|}, \tag{S7}$$

with s a dimensionless continuation parameter or pseudo-time and $\|\cdot\|$ the Euclidean length. The same equation appears as Eq. (20) of the main paper. The chosen parameter coordinates and scaling therefore define the flow. This is the substantive trade between the two updates. A geodesic of the FIM-induced metric is a coordinate-independent object, so the MBAM path is unchanged by a smooth reparameterization of the model. The smallest-eigenvalue direction of F_q carries no such invariance: expressing F_q in different coordinates rotates the eigenvector and moves the path. AS-MBAM therefore treats the coordinates as a declared input of the reduction, fixed here as the relative parameters $q_i = p_i/p_{0,i}$, which place the parameters on a common dimensionless scale about the local best fit. The consequences are confined to which candidates the search encounters, because each candidate limit is derived analytically and refitted independently before it is accepted; accuracy and identifiability are assessed on the refitted model.

S3.3 Bidirectional Candidate Generation and the Branching Tree

An eigenvector defines an axis with two initial orientations. We launch Eq. (S7) from both $+v_{\min}^{(q)}$ and $-v_{\min}^{(q)}$ because the branches can approach different limiting parameter combinations. Along each branch, the eigenvector sign is chosen to maintain a positive inner product with the preceding direction. At every retained child model, the two initial orientations are explored again, and multiple children may be retained under the adopted error criterion. A branch ends at an interpretable limit or when its error leaves the adopted range; the corresponding limit is then derived and refitted. Retained candidates seed the next reduction level, generating the tree in Fig. S1.

Near-degenerate soft eigenvalues can rotate the selected direction and expose additional branches. Future implementations will track the associated soft subspace automatically. For the X-57 continuation of Section S3.4, the two smallest eigenvalues of F_q differ by a factor of about 5 at the starting point, the smallest separation along the path; the ratio exceeds 10^3 by $s = 10$ and 10^6 at

the end of the continuation, so the selected soft direction is well separated throughout. The present tree contains the branch-terminal candidates reached under the adopted coordinates, continuation rules, and error criterion.

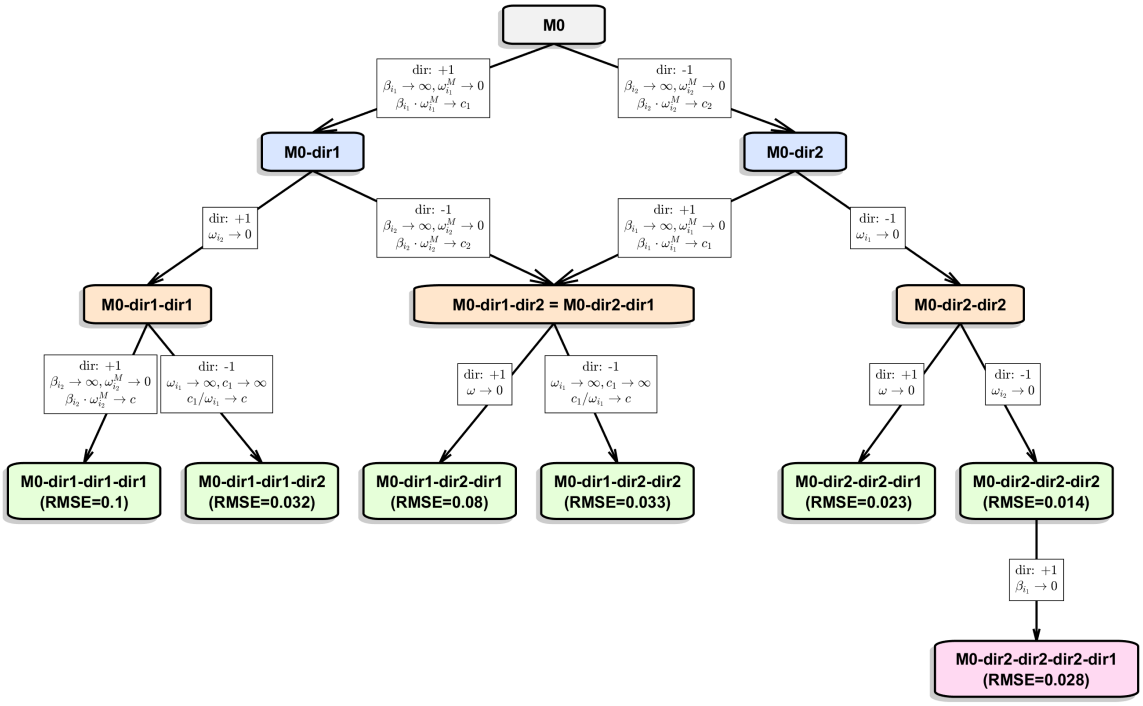


Figure S1: Toy-model branching hierarchy generated by the present AS-MBAM search from the seven-parameter (3L+1)pTROM (`M0`). Edges denote the two initial orientations of the local soft mode at each reduction step. Models with the same parameter count share a color. The retained branch-terminal candidates under the adopted error criterion are the four-parameter models `M0-dir1-dir1-dir2` (RMSE= 0.032), `M0-dir1-dir2-dir2` (RMSE= 0.033), and `M0-dir2-dir2-dir1` (RMSE= 0.023), and the three-parameter model `M0-dir2-dir2-dir2-dir1` (RMSE= 0.028). Table 2 of the main paper gives the corresponding limiting signatures.

S3.4 Application to the X-57 Six-Parameter Model

The six-parameter local ROM that starts the continuation documented here is derived in Section S4. The X-57 candidate structure was generated from one representative local fit for one brick and one temperature sensor. The two sensor outputs were used earlier in the coupled toy-model reduction. After the local ROM was derived, its sensor predictions decoupled, so the X-57 continuation could be performed on one representative sensor. The continuation documented here starts from the local best-fit six-parameter model

$$p = [A,\, B_a,\, \tilde{r},\, N_{Li,a},\, \alpha,\, \tau]^\top , \tag{S8}$$

and explores both orientations of the softest relative-coordinate mode.

Along the retained branch,

$$\alpha \to \infty, \qquad \tau \to 0, \qquad \gamma = \alpha\tau = \text{finite}. \tag{S9}$$

Let $Q(t) = \int_0^t I(t')\,dt'$. The thermal state equation can be written as

$$\tau \frac{d\Delta T}{dt} + \Delta T = \gamma Q(t). \tag{S10}$$

Equation (S9) is a fast-state singular-perturbation limit. In information-geometric language it lies on a boundary of the model manifold—the set of predictions generated as the parameters vary—because one dynamical state and one independent parameter disappear in the limit. Its engineering consequences are the simpler local thermal model used below and retention of the composite parameter γ, which carries the observable thermal gain into the limiting model. The limiting relation is

$$\Delta T = \gamma Q. \tag{S11}$$

The temperature-only trajectory diagnostic rises from approximately 0.007 to approximately 0.014 and then remains nearly flat over the observed continuation. Thus the candidate retains acceptable fit accuracy with a modest increase in this diagnostic. We derived the limiting model analytically, refitted it separately, and evaluated the resulting 5pTROM across the available X-57 brick–sensor records.

Within the explored continuation range, the opposite branch reached the adopted error threshold before approaching an interpretable limiting form and was terminated. A broader continuation of that branch can be examined in future work.

The τ in Eqs. (S9) and (S10) is an internal effective cell-to-matrix relaxation time. It is distinct from the external sub-module cooling time $\tau_{\text{ext}} \approx 6.7\,\text{h}$ in Eq. (S3), which supports the quasi-adiabatic external boundary condition.

The single-sensor continuation generated the candidate model form, which was subsequently refitted independently across all brick–sensor pairs. The pack-wide fits test the accuracy and diagnostic content of the common local structure across the available X-57 data.

S3.5 State and First-Order Sensitivity Equations, Relative Scaling, and the Discrete Metric

The continuation calculation uses the cathode intercalation state $x(t) = \bar{x}_c(t)$ and the local temperature rise $T(t) = \Delta T(t)$. With $N = N_{Li,a}$ and $V_0 = V(0)$, the predicted current and state equations are

$$I(t) = \frac{A + (V_0 - A)x + B_a \log x - V(t)}{\tilde{r}}, \tag{S12}$$

$$\dot{x} = f_x = -\frac{I}{eN}, \qquad \dot{T} = f_T = \alpha e N(1 - x) - \frac{T}{\tau}. \tag{S13}$$

The initial conditions are $x(0) = 1$ and $T(0) = 0$. Here $T(0)$ denotes the second raw temperature sample; the first sample is corrupted and is excluded.

For each physical parameter p_j, define the state-sensitivity vector

$$S_j(t) = \begin{bmatrix} \partial x/\partial p_j \\ \partial T/\partial p_j \end{bmatrix}. \tag{S14}$$

It satisfies the first-order linear system

$$\dot{S}_j = A_s S_j + g_j, \qquad S_j(0) = 0, \tag{S15}$$

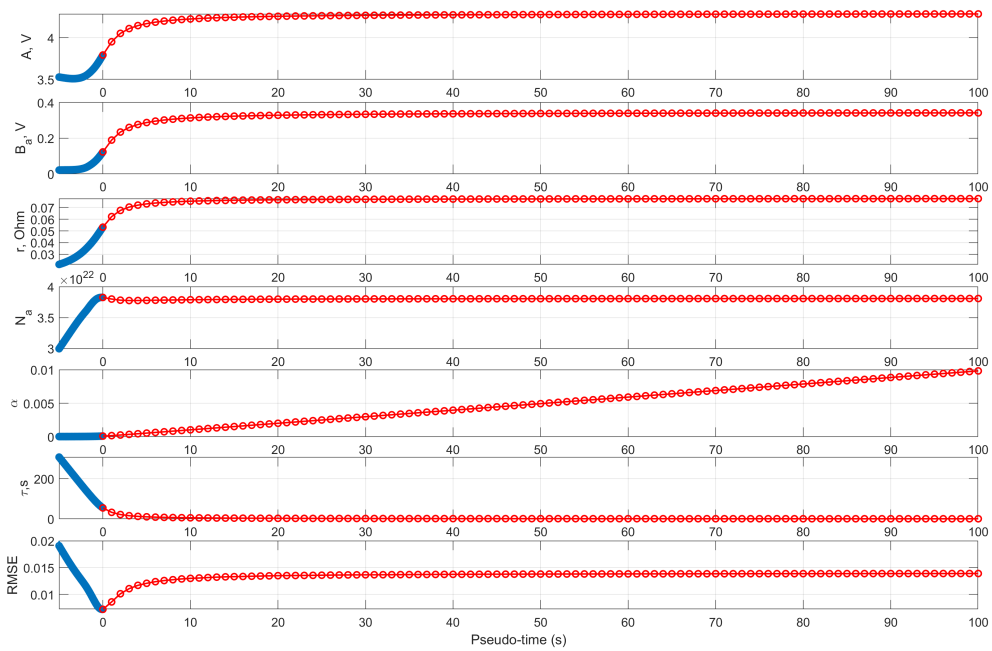


Figure S2: Evolution of the six-parameter X-57 local ROM along the two AS-MBAM continuations. Red markers show the retained $+v_{\min}^{(q)}$ branch leading to the 5pTROM. Blue markers show the explored $-v_{\min}^{(q)}$ branch, which crossed the adopted error threshold before reaching a retained limiting model. The horizontal coordinate is the dimensionless continuation parameter s of Eq. (S7). Along the retained branch, $\alpha \to \infty$ and $\tau \to 0$ while $\gamma = \alpha\tau$ remains finite; the temperature-only trajectory diagnostic rises from approximately 0.007 to approximately 0.014 and then remains nearly flat. Along the blue branch, the diagnostic leaves the adopted acceptance range before an interpretable limiting form is reached.

where

$$A_s = \begin{bmatrix} -\dfrac{V_0 - A + B_a/x}{eN\tilde{r}} & 0 \\ -\alpha eN & -1/\tau \end{bmatrix}. \tag{S16}$$

For the ordered parameter vector in Eq. (S8), the explicit forcing columns form

$$G = \begin{bmatrix} g_1 & \cdots & g_6 \end{bmatrix} = \begin{bmatrix} -\dfrac{1-x}{eN\tilde{r}} & -\dfrac{\log x}{eN\tilde{r}} & \dfrac{I}{eN\tilde{r}} & \dfrac{I}{eN^2} & 0 & 0 \\ 0 & 0 & 0 & \alpha e(1-x) & eN(1-x) & T/\tau^2 \end{bmatrix}. \tag{S17}$$

The temperature Jacobian is obtained directly from the second component of S_j. The current Jacobian follows from Eq. (S12):

$$\frac{\partial I}{\partial p_j} = \frac{V_0 - A + B_a/x}{\tilde{r}} \frac{\partial x}{\partial p_j} + h_j, \qquad h = \left[\frac{1-x}{\tilde{r}}, \frac{\log x}{\tilde{r}}, -\frac{I}{\tilde{r}}, 0, 0, 0 \right]. \tag{S18}$$

Evaluating these sensitivities at the common sample times gives the physical-coordinate blocks $J_{T,p}$ and $J_{I,p}$.

The continuation uses dimensionless relative parameters

$$q_i = \frac{p_i}{p_{0,i}}, \qquad J_{T,q} = J_{T,p}\,\mathrm{diag}(p_0), \qquad J_{I,q} = J_{I,p}\,\mathrm{diag}(p_0), \tag{S19}$$

where p_0 is the local best-fit vector. This chain-rule scaling removes the dimensional inconsistency of applying a Euclidean norm directly to heterogeneous physical parameters. It also defines the coordinates on which the trajectory depends.

Let N_s denote the number of common time samples used for the current and temperature sensitivity blocks. Define

$$T_{\mathrm{rms}} = \left(\frac{1}{N_s} \sum_{n=1}^{N_s} T_{\mathrm{meas},n}^2 \right)^{1/2}, \qquad I_{\mathrm{rms}} = \left(\frac{1}{N_s} \sum_{n=1}^{N_s} I_{\mathrm{meas},n}^2 \right)^{1/2}. \tag{S20}$$

The exact discrete dimensionless metric used to select the AS-MBAM direction is

$$F_q = \frac{J_{T,q}^\top J_{T,q}}{T_{\mathrm{rms}}^2} + (0.03)^2 \frac{J_{I,q}^\top J_{I,q}}{I_{\mathrm{rms}}^2}. \tag{S21}$$

Thus the current contribution has weight

$$w_I = (0.03)^2 = 9 \times 10^{-4} \simeq 10^{-3}. \tag{S22}$$

The metric contains both temperature and current sensitivities. The temperature-only error displayed along the trajectory is instead

$$\epsilon_{T,\mathrm{traj}} = \left[\frac{\sum_{n=1}^{N_s} \left(T_{\mathrm{pred},n} - T_{\mathrm{meas},n} \right)^2}{\sum_{n=1}^{N_s} T_{\mathrm{meas},n}^2} \right]^{1/2}. \tag{S23}$$

Equation (S23) is an RMS-normalized, temperature-only diagnostic. It uses the same RMS normalization as the temperature term of the fit costs, and it is distinct from the sensitivity metric in Eq. (S21) and from the absolute temperature residuals (in °C) reported for the pack-wide fits.

S4 Intermediate Per-Sensor ROMs for the X-57 Data

This section gives the detail behind the summary in Section 6 of the main paper: how the structural scaling degeneracy of the per-sensor model is resolved, and how the seven-parameter model reduces to the six-parameter ROM that starts the AS-MBAM continuation of Section S3.4.

S4.1 Resolution of the Structural Non-Identifiability

For the X-57 pack-wide evaluation we work per sensor: each thermal sensor on each brick is fitted with its own local model, with no parameters shared across sensors or bricks. Coupling the two-parameter local thermal model, Eq. (21) of the main paper, to the six-parameter electrochemical model of Section 4.2 of the main paper gives eight parameters per sensor: the electrochemical parameters A, B_c, B_a, $\tilde{r}$, $N_{Li,a}$ and τ_a, and the local thermal parameters $\alpha \equiv \omega^M \beta$ and $\tau \equiv 1/\omega^M$. The fitted thermal output is the local temperature rise relative to the first reliable temperature record: the first raw record is corrupted, so the second raw temperature sample defines the reference $T^M(0)$ and $\Delta T^M(t) \equiv T^M(t) - T^M(0)$. The thermal model is therefore parameterized as

$$\frac{d\Delta T^M}{dt} = \alpha \int_0^t I(t')\, dt' - \frac{1}{\tau} \Delta T^M. \tag{S24}$$

The initial condition $A + B_c = V(0)$, where $V(0)$ is the known voltage of a fully charged cell, fixes one of the electrochemical parameters and reduces the number of independent parameters per sensor

to seven; without loss of generality we choose A as an independent parameter and let B_c be fixed by the initial condition.

A further challenge arises from the model's structure. In the absence of direct cell-current measurements the model is structurally non-identifiable: the predicted matrix temperature T^M is invariant under the scaling transformation

$$N_{Li,a} \to c\, N_{Li,a}, \qquad \tilde{r} \to \tilde{r}/c, \qquad \alpha \to \alpha/c \tag{S25}$$

for any constant c. This transformation scales the predicted current as $I(t) \to c\, I(t)$ while leaving the predicted temperature unchanged. To resolve the scaling ambiguity we use the available current data: only the total current of a pack is measured, but because the 128 bricks of a pack form a single series chain, the average current per cell within a parallel-connected brick is a reasonable proxy for the local cell current under the assumption of moderate cell-to-cell variation. Adding the normalized mean square error (MSE) of the current to the normalized MSE for temperature in the optimization cost function[1] resolves the ambiguity. For a sufficiently small weight on the current MSE term, the best-fit parameter values are expected to be independent of the specific weight chosen.

We performed a multi-start optimization for a single sensor's data using two different small weights, 0.001 and 0.005, for the current MSE, with cost $(\mathrm{MSE}_T + w\,\mathrm{MSE}_I)^{1/2}$. Each multi-start set comprises 100 runs of the Nelder–Mead simplex algorithm (MATLAB `fminsearch`; at most 5000 iterations and 20000 function evaluations, tolerances 10^{-8}), each started from parameters drawn independently and uniformly within $\pm 60\%$ of a nominal vector. Runs that left the physical domain, signaled by a complex-valued cost, were discarded. The data are the first 2060 s of the record, resampled to 300 uniform points. The pack-wide 5pTROM fits of the main text use the same algorithm, settings, and data preparation with ten starts per brick–sensor pair. The resulting distributions for the seven fitted parameters are shown in Figure S3. The distributions for the two weights are very similar, confirming that the method breaks the structural invariance robustly. The distributions for most parameters are broad even for fits with very low RMSE, indicating that the model, while accurate, remains sloppy with respect to the available data.

S4.2 The $\tau_a \to 0$ Limit and the Six-Parameter ROM

In the seven-parameter per-sensor fit (A, B_a, $\tilde{r}$, $N_{Li,a}$, τ_a, α and τ) of Figure S3, the anode diffusion time constant τ_a takes values ranging over orders of magnitude, with many of the best fits as small as 10 ms—a timescale much shorter than any relevant scale of temperature variation in the system. The fitted outputs provide little sensitivity to solid-state diffusion dynamics: the temperature, which dominates the cost, integrates the current, and the weakly weighted brick-average current proxy does not resolve diffusion transients. The optimizer is therefore free to drive τ_a toward zero. The limit $\tau_a \to 0$ is a data-driven identifiability boundary induced by the information content of the measurements and represents the diffusion dynamics at the resolution of this experiment.

Taking $\tau_a \to 0$ simplifies the electrochemical model: the unobservable solid-phase anode diffusion is projected out, and the apparent surface lithium concentration equals the bulk concentration at all times for this loading profile. Eqs. (11) and (12) of the main paper then give $\bar{x}_a(t) = \bar{x}_c(t)$, and the model reduces to a six-parameter ROM in A, B_a, $\tilde{r}$, $N_{Li,a}$, α and τ.

The results of fitting the six-parameter ROM are shown as green dots in Figure S3. The reduction is effective: the six-parameter model is almost as accurate as the seven-parameter version, with the

[1] Each MSE was normalized by the mean-square value of the corresponding measured signal over the fitted window; the temperature signal is the rise above the reference $T^M(0)$, and the current signal is the brick-average current per cell, the measured pack current divided by 20.

minimum RMSE increasing only from 0.006 to 0.007. The distributions for α and B_a still vary significantly at low RMSE, so the model remains sloppy and admits further reduction. This six-parameter ROM is the starting point of the AS-MBAM continuation documented in Section S3.4.

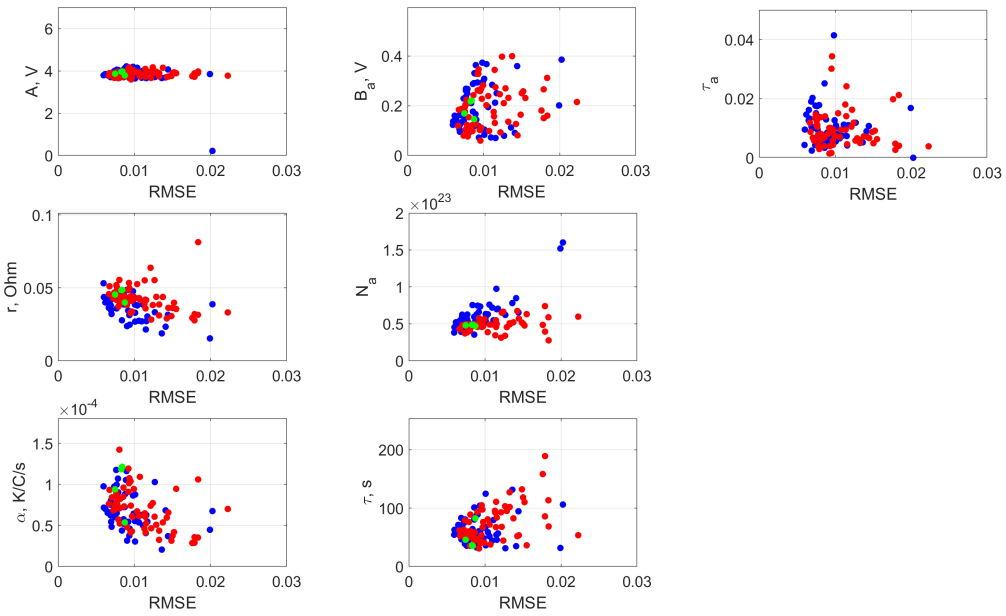


Figure S3: Distributions of the fitted parameters versus Root Mean Square Error (RMSE), calculated with respect to the temperature data only. Blue and red dots correspond to the seven-parameter model with current MSE weights of 0.001 and 0.005, respectively. Green dots show the results for the reduced six-parameter ROM, where $\tau_a \to 0$. The parameters shown are the electrochemical parameters A, B_a, τ_a, $\tilde{r}$ (labeled as r) and $N_{Li,a}$, and the local thermal parameters α and τ. The six-parameter ROM omits τ_a.

References

[1] D. Hernandez-Lugo, S. Clarke, T. Miller, M. Redifer, T. Foster, X-57 Maxwell Battery from Cell Level to System Level Design and Testing, NASA Technical Reports Server (2018).
URL https://ntrs.nasa.gov/citations/20180005737

[2] Z. Hashin, S. Shtrikman, A variational approach to the theory of the effective magnetic permeability of multiphase materials, Journal of Applied Physics 33 (10) (1962) 3125–3131. doi:10.1063/1.1728579.

[3] S. W. Churchill, H. H. S. Chu, Correlating equations for laminar and turbulent free convection from a vertical plate, International Journal of Heat and Mass Transfer 18 (11) (1975) 1323–1329. doi:10.1016/0017-9310(75)90243-4.

[4] M. K. Transtrum, P. Qiu, Model reduction by manifold boundaries, Physical Review Letters 113 (9) (2014) 098701. doi:10.1103/physrevlett.113.098701.
URL https://doi.org/10.1103/physrevlett.113.098701

[5] M. K. Transtrum, B. L. Francis, C. C. Youn, A. T. Saric, A. M. Stankovic, Geometrically motivated reparameterization for identifiability analysis in power systems models, in: 2018 North American Power Symposium (NAPS), IEEE, 2018. doi:10.1109/naps.2018.8600617.
URL https://doi.org/10.1109/naps.2018.8600617

[6] K. N. Quinn, M. C. Abbott, M. K. Transtrum, B. B. Machta, J. P. Sethna, Information geometry for multiparameter models: new perspectives on the origin of simplicity, Reports on Progress in Physics 86 (3) (2022) 035901. doi:10.1088/1361-6633/aca6f8.
URL https://doi.org/10.1088/1361-6633/aca6f8